An Improved Thin-Wire Model for FDTD

Riku M. Mäkinen, *Member, IEEE*, Jaakko S. Juntunen, *Member, IEEE*, and Markku A. Kivikoski, *Member, IEEE*

***Abstract*—An improved thin-wire model for the finite-difference time-domain method is proposed. The new model can be used to accurately model straight wire sections connected to other metal structures. In addition, the model includes the effect of charge accumulation at wire end caps. The end-cap model is based on conservation of charge and Coulomb's law. Using the end-cap model, unconnected wires such as wire antennas are also accurately modeled. The results indicate a significant improvement in predicting the resonance frequency of a dipole antenna.**

***Index Terms*—FDTD, sub-cell model, thin-wire model.**

I. Introduction

SUB-CELL models are used in finite-difference time-domain (FDTD) method to describe small geometrical details without resorting to a large number of smaller cells. Sub-cell thin-wire models are widely used in antenna problems such as modeling of wire antennas or as a part of the antenna or waveguide feed structure. In either case, the computed input impedance or scattering parameters are affected by the accuracy of the thin-wire model. In addition to the wire radius, accurate modeling of wire length should be considered if the wire ends are not connected to other structures.

In the standard thin-wire model [1] static field distribution is assumed for the scattered field components adjacent to the wire. The sub-cell geometry of a wire is modeled using the contour-path integral formulation of FDTD. Modifications to the standard model have been proposed, such as in [2], where further assumptions on the field distribution near the wire ends are made. A different approach is presented in [3], where FDTD is formulated as the time-domain finite-element method, and static field solutions are incorporated by modifying the basis functions near the wire.

A filamentary hard source and a filamentary perfect electric conductor (PEC) wire implemented by setting an electric field component on a wire axis identically to zero are known to have a finite effective radius r_{eff}. A method to obtain r_{eff} of a two-dimensional (2-D) filamentary hard source was presented in [4]. By comparison to a frequency-domain Green's function, the value of r_{eff} was found to be between 0.206Δ and 0.209Δ, where Δ is the cell size. Due to the fact that a filamentary PEC wire is effectively a hard source with the excitation function identically set to zero, the procedure of [4] can be used to test the accuracy of a 2-D thin-wire model. This is done in [5], where it is shown that the standard thin-wire model [1] does not model the wire radius accurately in 2-D.

In addition to accurate modeling of the wire radius, modeling of wire ends has a profound effect on the overall accuracy in modeling of wire antennas. Both the standard wire model and the three-dimensional (3-D) version of [5] have been shown to suffer from the coarseness error affecting the length of the wire [6]. A considerable improvement compared to the standard thin-wire model was achieved by introducing further assumptions on the field distribution at the antenna ends based on NEC-computed data [2]. However, only the wire ends are considered in [2].

In [5], a 2-D thin-wire model that accurately describes the wire radius was proposed. The 2-D model reduces to a filamentary PEC wire when the nominal wire radius is set to $e^{-\pi/2}\Delta \approx 0.208\Delta$, which is in agreement with the result given in [4]. In this paper, the 2-D thin-wire model of [5] is extended into three dimensions. In addition, an algorithm to model the wire end caps is proposed. Instead of using precomputed field distributions for field components near wire ends, as in [2], we begin with similar assumptions that are used in NEC-4 to model the wire end caps [7]. The proposed model describing the effect of charge accumulation at the wire ends is based on conservation of charge and Coulomb's law.

II. Improved Thin-Wire Model

The proposed model is based on the contour-path integral formulation of FDTD, where the integral form of Ampere's law and Faraday's law are enforced locally in each Yee cell [1]. The Ampere's law in free space is given by

$$\int_{S_d} \frac{\partial}{\partial t} \varepsilon_0 \mathbf{E} \cdot d\mathbf{S}_d = \oint_{C_d} \mathbf{H} \cdot d\mathbf{l}_d \tag{1}$$

where surface S_d is a dual-grid cell facet bounded by contour C_d formed by dual-grid cell edges. Similarly, the Faraday's law in free space is given by

$$-\int_{S_p} \frac{\partial}{\partial t} \mu_0 \mathbf{H} \cdot d\mathbf{S}_p = \oint_{C_p} \mathbf{E} \cdot d\mathbf{l}_p \tag{2}$$

where surface S_p is a primary-grid cell facet bounded by contour C_p formed by primary-grid cell edges.

The basic idea in the standard thin-wire model [1] is that it incorporates static field solution into FDTD. This is also the case with the proposed model. While the static field distribution is only used as an approximation, it is consistently enforced on all field components involved in the wire models [8].

Manuscript received December 28, 2000. This work was supported in part by the Finnish Graduate School for Electronics, Telecommunications, and Automation and in part by the Nokia Foundation.

R. M. Mäkinen and M. A. Kivikoski are with the Institute of Electronics, Tampere University of Technology, FIN-33101 Tampere, Finland (e-mail: riku.makinen@tut.fi; markku.kivikoski@tut.fi).

J. S. Juntunen was with the Radio Laboratory, Helsinki University of Technology, FIN-02015 TKK, Finland. He is now with the Aplac Solutions Corporation, FIN-00370 Helsinki, Finland (e-mail: jaakko.juntunen@aplac.com).

Publisher Item Identifier S 0018-9480(02)04067-X.

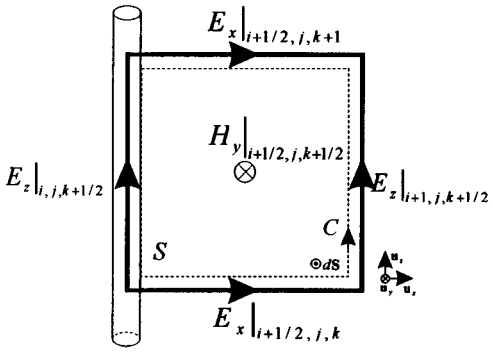

Fig. 1. Faraday's law integration path for the looping magnetic field components adjacent to a wire [1].

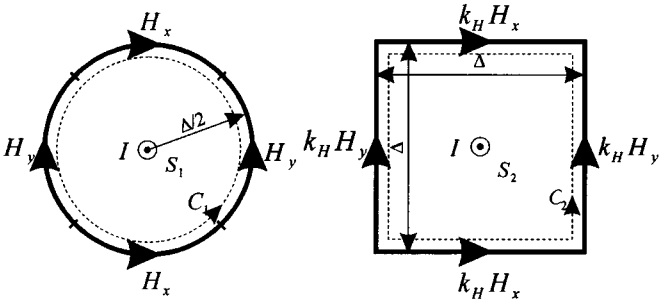

Fig. 2. Circular Ampere's law integration path C_1 for a $1/r$ dependent tangential magnetic field circulating the wire [5]. The field components are projected onto the Cartesian cell edge on C_2 prior to being used in the standard FDTD update equations.

A. Looping Magnetic Field Components

Derivation of the looping magnetic field components adjacent to the wire follows the derivation of a 2-D TM-mode thin-wire model [5]. Let us consider computation of one of the four looping magnetic field components adjacent to a wire, as shown in Fig. 1. The looping magnetic field and the radial electric field are assumed $1/r$ dependent in the radial direction, where r is the distance from the wire axis. For example, an update equation for the looping magnetic field at $(i+1/2,\, j,\, k+1/2)$ can be found using (2). Assuming free space, we have [1]

$$\begin{aligned} H_y|^{n+1/2}_{i+1/2,\,j,\,k+1/2} &= H_y|^{n-1/2}_{i+1/2,\,j,\,k+1/2} \\ &\quad - \frac{\Delta t}{\mu_0 \Delta z}\left[E_x|^{n}_{i+1/2,\,j,\,k+1} - E_x|^{n}_{i+1/2,\,j,\,k}\right] \\ &\quad + \frac{2\Delta t}{\mu_0 \Delta x \ln(\Delta x/a)}\left[E_z|^{n}_{i+1,\,j,\,k+1/2} - E_z|^{n}_{i,\,j,\,k+1/2}\right] \end{aligned} \tag{3}$$

where a is the nominal radius of the wire. Note that H_y in (3) represents the tangential magnetic field along a circular path around the source, as shown in Fig. 2(a). Using a point value such as H_y in (3) in standard FDTD update equations is in contradiction with the assumption that H_y should represent the average value of the field along the Cartesian dual-grid cell edge.

In order to avoid this inconsistency, we project the looping magnetic field components onto the respective Cartesian cell edges prior to using them in the standard FDTD equations [2], [3], [5]. Let us assume we have computed any of the magnetic field components H in Fig. 2(a) using (3). In order to project H into $k_H H$ on a Cartesian cell edge, as shown in Fig. 2(b), we use Ampere's law as a starting point. Forming two integration paths C_1 and C_2 around the wire, we have

$$I = \oint_{C_1} \mathbf{H}\cdot d\mathbf{l}_1 = \oint_{C_2} \mathbf{H}\cdot d\mathbf{l}_2. \tag{4}$$

For a rotationally symmetric case, the magnetic field is constant along C_1. The scaling factor k_H is determined by the relative length of the integration paths C_1 and C_2

$$k_H = \oint_{C_1} d\mathbf{l}_1 \Big/ \oint_{C_2} d\mathbf{l}_2 = \pi/4. \tag{5}$$

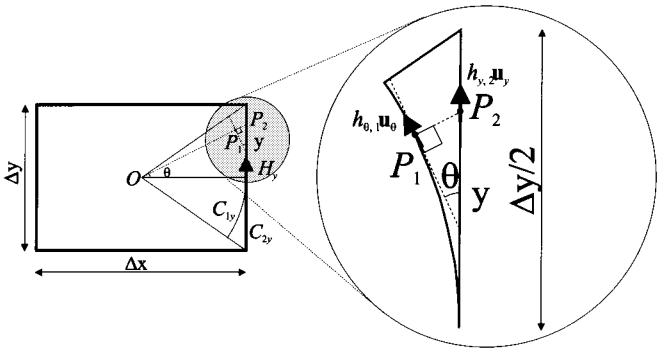

Fig. 3. Cross-sectional view of a nonuniform cell for computation of the scaling factor k_H for the magnetic field component H_y. The wire axis is located at origin O. A magnified view of the shaded area is shown on the right-hand side.

In a nonsymmetric case, values of the four looping magnetic field components may differ from each other due to reflections from other structures. Still, we may define a scaling factor for each segment such that the line integral of $\mathbf{H}$ along each circular segment remains equal to the line integral of $\mathbf{H}$ along the respective Cartesian dual-grid cell edge, i.e.,

$$k_{H,i} = \int_{C_{1i}} d\mathbf{l}_1 \Big/ \int_{C_{2i}} d\mathbf{l}_2\,. \tag{6}$$

Here, we assume H and $k_H H$ are constant on each of the four segments of C_1 and C_2, respectively.

The shape of the cells affects the value of k_H. A cross-sectional view of a cell with $\Delta x \neq \Delta y$ is shown in Fig. 3. In order to compute the scaling factor for H_y, the looping magnetic field component along a segment of the circle C_{1y} at distance $\Delta x/2$ from the wire axis is projected to the Cartesian cell edge C_{2y}. Due to symmetry, we only need to consider half of the cell edge shown magnified in Fig. 3. Let us consider projection of the looping magnetic field at point P_1 on C_{1y} to the magnetic field along the Cartesian cell edge at point P_2 on C_{2y}. Due to the $1/r$ dependence, the amplitude of the magnetic field is decreased by a factor of $|OP_1|/|OP_2|$. The direction of the magnetic field $h_{\theta,1}\mathbf{u}_\theta$ at P_1 is tangential to the path C_{1y}. The y component required in FDTD is obtained by projecting the tangential field component to the y-direction, i.e.,

$h_{y,1} = h_{\theta,1}\mathbf{u}_\theta \cdot \mathbf{u}_y = h_{\theta,1}\cos\theta$. Integrating over C_{2y} and dividing by the length of path C_{2y}, we have

$$k_{Hy} = \frac{1}{\Delta y/2}\int_0^{\Delta y/2} \cos\theta \frac{(\Delta x/2)}{\sqrt{(\Delta x/2)^2 + y^2}}\, dy \qquad (7)$$

where $\cos\theta$ projects the tangential magnetic field in the y-direction and the second term in the integrand is the attenuation of the field due to an increase in the distance from the wire axis. Integrating (7) gives

$$k_{Hy} = (\Delta x/\Delta y)\cdot \tan^{-1}(\Delta y/\Delta x). \qquad (8)$$

The scaling factor k_{Hx} for H_x is obtained in a similar manner and is given by

$$k_{Hx} = (\Delta y/\Delta x)\cdot \tan^{-1}(\Delta x/\Delta y). \qquad (9)$$

Instead of scaling the value of the magnetic field H, we use the scaled value $k_H H$ in standard FDTD update equations to compute the adjacent electric field components.

B. Radial Electric Field Components

The radial electric field components adjacent to the wire are computed using the standard FDTD update equations. However, the scaled values (e.g., $k_H H_y$) of the looping magnetic field components are used. For example, the radial electric field component at $(i+1/2,\ j,\ k)$ is given by

$$\begin{aligned} E_x|^{n+1}_{i+1/2,\,j,\,k} &= E_x|^{n}_{i+1/2,\,j,\,k} \\ &\quad - \frac{\Delta t}{\varepsilon_0 \Delta z}\left[k_H H_y|^{n+1/2}_{i+1/2,\,j,\,k+1/2} - k_H H_y|^{n+1/2}_{i+1/2,\,j,\,k-1/2}\right] \\ &\quad + \frac{\Delta t}{\varepsilon_0 \Delta y}\left[H_z|^{n+1/2}_{i+1/2,\,j+1/2,\,k} - H_z|^{n+1/2}_{i+1/2,\,j-1/2,\,k}\right] \end{aligned} \qquad (10)$$

where k_H projects the looping magnetic field components to a Cartesian cell edge. The radial electric field E_x computed using (10) represents the average value for the electric field flowing through a Cartesian cell facet S_1, as shown in Fig. 4. The computed value can be directly used in the standard FDTD update equations to compute the adjacent axial magnetic field components. However, in order to compute a looping magnetic field component, as shown in Fig. 1, a $1/r$ dependent radial electric field point value is required instead of an average electric field through a Cartesian cell facet.

In order to obtain a point value for the radial electric field at distance $\Delta/2$ from the wire axis, the radial electric field component is projected from a Cartesian cell facet S_1 to a cylindrical surface S_2, as shown in Fig. 4. Due to the $1/r$ assumption, the radial electric field is also constant on surface S_2. Keeping the surface integral of E_x unchanged, the scaling factor k_E required to project the electric field to the cylindrical surface S_2 is simply determined by the ratio of areas of S_1 and S_2 as follows:

$$k_E = \int_{S_1} d\mathbf{s}_1 \Big/ \int_{S_2} d\mathbf{s}_2\ . \qquad (11)$$

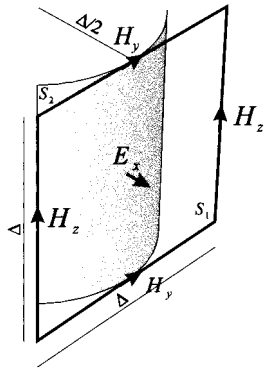

Fig. 4. Cylindrical Ampere's law integration surface S_2 for a $1/r$ dependent radial electric field component adjacent to the wire. The field component is projected from the Cartesian cell facet S_1 to the cylindrical surface S_2 prior to being used in thin-wire update equations.

Due to the fact that Δz is equal on both surfaces S_1 and S_2, the scaling factor k_E for the radial electric field is determined by the transverse cell dimensions

$$k_{Ex} = \left[(\Delta x/\Delta y)\cdot \tan^{-1}(\Delta y/\Delta x)\right]^{-1} \qquad (12)$$

$$k_{Ey} = \left[(\Delta y/\Delta x)\cdot \tan^{-1}(\Delta x/\Delta y)\right]^{-1} \qquad (13)$$

which both reduce to $4/\pi$ when $\Delta x = \Delta y$.

As with the scaling factor for the looping magnetic field components discussed in Section II-A, the radial electric field components themselves are not scaled. Instead, the scaled field values are used in computation of the looping magnetic field components.

C. Axial Electric Field Components

The axial electric field components within the perfectly conducting wire are identically set to zero. As a field component in FDTD represents the average value of that field through the cell facet, zero axial electric field is enforced throughout the cell. As a consequence, no displacement current is allowed to flow in the axial direction and an assumption of static field distribution is, therefore, enforced.

Connecting a source on a wire described by thin-wire equations is discussed in [8]. It is shown that the assumptions on field distribution enforced in a delta-gap hard source [9] are consistent with those enforced in both the standard model [1] and in the proposed model. As a consequence, thin-wire equations can be freely applied to a cell containing a hard source. No scaling factor such as k_H or k_E is used for the axial electric field excited by a hard source. This is due to the fact that the area of the cell facet the axial electric field flows through is not used in any of the update equations. Therefore, no scaling based on area is required. Note that while the axial electric field at the source is a function of time, no displacement current flows through the cell because the change in the axial electric field does not contribute to the computation of any of the adjacent field components.

The resistive voltage source (RVS) [10], [11] allows displacement current to flow through the source cell. This is in contradiction with the assumption of static fields enforced in thin-wire equations. Consequently, limitations in a stable range of values

for wire radius a or time step Δt result if either standard or revised thin-wire equations are used in a cell containing an RVS [8]. It is likely that the problem is related to correctly defining the axial electric field distribution for both the RVS and wire model simultaneously.

A direct consequence of a nonzero displacement current is that, for the proposed model, (4) does not hold. However, as an approximation, one can form the Ampere's law integral equations over S_1 and C_1 in Fig. 2(a) when deriving RVS update equations, and apply thin-wire equations (10) and (14) as usual. This results in similar stability constraints that are observed when directly combining the standard wire model and RVS [8].

D. Thin-Wire Update Equations

The update equation for the radial electric field components is given in (10). However, the update equation for the magnetic field components looping the wire is slightly modified from (3) by including the scaling factor k_E of (11). For example, the looping magnetic fieldH_y at $(i+1/2,\ j,\ k+1/2)$ is given by

$$\begin{aligned} H_y|^{n+1/2}_{i+1/2,\,j,\,k+1/2} &= H_y|^{n-1/2}_{i+1/2,\,j,\,k+1/2} \\ &\quad - \frac{\Delta t}{\mu_0 \Delta z}\left[k_E E_x|^{n}_{i+1/2,\,j,\,k+1} - k_E E_x|^{n}_{i+1/2,\,j,\,k}\right] \\ &\quad + \frac{2\Delta t}{\mu_0 \Delta x \ln(\Delta x/a)}\left[E_z|^{n}_{i+1,j,k+1/2} - E_z|^{n}_{i,j,k+1/2}\right] \end{aligned} \tag{14}$$

where $k_E E_x$ is the $1/r$ dependent radial electric field. As stated earlier, the computed magnetic field H_y represents the $1/r$ dependent looping magnetic field at distance $\Delta/2$ from the wire and the scaled value $k_H H_y$ should be used in computation of all adjacent electric field components.

Scaling factors k_H and k_E used in (10) and (14), respectively, are the only modification to the standard thin-wire model [1] required for a wire with both ends connected to other metal structures. However, if the wire ends are unconnected, as is the case in a wire antenna or the tip of a coaxial probe, the wire ends also need to be considered.

III. Wire End Caps

A. Wire End-Cap Model

The basic principle of the proposed wire end-cap model is similar to that used in frequency-domain method of moments (MoM) code NEC-4 [7]. Let us consider a half-wave dipole in free space. The current is zero at the antenna ends only if the antenna is very thin. However, with a finite wire radius, a small current is allowed to flow to the antenna end caps. As a result, charge is accumulated at the antenna ends. The simplest approximations for the charge distribution on the end cap are the uniform surface charge distribution used in [7] and the uniform line charge distribution along the edge of the end cap. Both approximations are valid and either one of them could be chosen. In fact, the effect on the wire model turned out to be practically identical for the two charge distributions. However, the line charge distribution results in more compact expressions for the electric field due to the charged end cap and is, therefore, adopted in the proposed model.

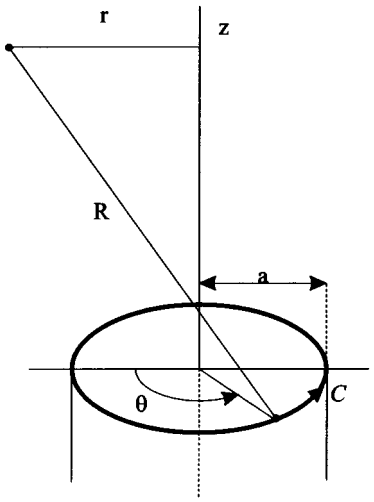

Fig. 5. Geometry for evaluation of the field due to a charged end cap. The geometry is similar to that used for a uniform surface charge density in [7].

Conservation of charge requires that at wire end [12]

$$\int_S \mathbf{J}\cdot\mathbf{n}\,da = -\frac{d}{dt}\int_C \rho\,dl \tag{15}$$

where $\mathbf{J}$ is the current density at the wire end and ρ is the line charge density on the edge of the end cap. Assuming static field distribution, potential ϕ due to ρ is given by Coulomb's law [12]

$$\phi = \frac{1}{4\pi\varepsilon_0}\int_C \frac{\rho}{R}\,dl \tag{16}$$

where R is the distance from a point within the line charge distribution on C to the observation point, and C is the path enclosing the end cap of the wire. The electric field due to the charge accumulated at the wire ends is computed from the potential using

$$\mathbf{E} = \nabla\phi. \tag{17}$$

The FDTD implementation of the model for the end caps requires further approximations. Let us consider the top end of a wire in the z-direction, as shown in Fig. 5. The current at the end of the wire is not available in FDTD. It is, therefore, approximated with the current at half a cell below the wire end. Note that the current must travel half a cell distance to reach the wire end in order to contribute to the surface charge at the end cap. In addition, it takes a finite time for the electric field due to the charge to reach the observation point [13]. However, it was found that retarding the field does not significantly affect the results and was, therefore, not included in model. The change Δq in the total charge q at the wire end is computed using (15). Assuming the current constant for the duration of each time step Δt, we have

$$\Delta q = -I|^{n+1/2}_{k_{\rm top}-1/2}\,\Delta t \tag{18}$$

where the current I is computed from the circulation of the magnetic field around the wire at half a cell below the wire end.

The electric potential due to the charged end cap is computed using Coulomb's law resulting in

$$\phi(r,z) = \frac{1}{4\pi\varepsilon_0}\int_0^{2\pi}\frac{\rho}{R}a\,d\theta \tag{19}$$

where a is the wire radius, R is the distance from a point within the charge distribution to the observation point, and line charge density is given by $\rho = \Delta q/2\pi a$. Using the notation of Fig. 5, the distance R from the line charge to the observation point is given by

$$R = \sqrt{r^2 + a^2 - 2ra\cos\theta + z^2} \tag{20}$$

where r is the distance from the wire axis, z is the distance from the wire end in the axial direction, a is the radius of the wire, and θ is the angle in the transverse plane between r and a. Solving the integral in (16) gives

$$\phi(r,\,z) = \frac{1}{4\pi\varepsilon_0}\,\frac{\Delta q}{2\pi a}\,\frac{4aK(k)}{\sqrt{(r+a)^2+z^2}} \tag{21}$$

where Δq is the charge computed using (18), K is a complete elliptic integral of the first kind, and

$$k = \frac{2\sqrt{ar}}{\sqrt{(r+a)^2+z^2}}. \tag{22}$$

The electric field due to the charged wire end cap is obtained from potential using (17). However, in FDTD, we need to separate the axial-field component and the radial-field component. The axial electric field is given by

$$E_{z,\,q}(r,\,z) = -\frac{\partial\phi(r,\,z)}{\partial z}. \tag{23}$$

Similarly, the radial electric field is given by

$$E_{r,\,q}(r,\,z) = -\frac{\partial\phi(r,\,z)}{\partial r}. \tag{24}$$

Solving (23) gives

$$E_{z,\,q} = \frac{\Delta q}{4\pi\varepsilon_0}\,\frac{zE(k)}{2\pi\left((r-a)^2+z^2\right)\sqrt{(r+a)^2+z^2}} \tag{25}$$

where E is a complete elliptic integral of the second kind and k is given by (22). Solving (24) gives outside the wire axis

$$E_{r,\,q} = \frac{\Delta q}{4\pi\varepsilon_0}\,\frac{\left((r-a)^2+z^2\right)K(k) - \left(-r^2+a^2+z^2\right)E(k)}{\pi r\left((r-a)^2+z^2\right)\sqrt{(r+a)^2+z^2}} \tag{26}$$

where K is a complete elliptic integral of the first kind, E is a complete elliptic integral of the second kind, and k is given by (22).

According to (16), we need the total charge at the wire end to compute the electric potential due to the charge. However, in (25) and (26), we only use the change in the total charge at the wire end. This is because in FDTD the change in electric field is computed at each time step, and the contribution of the accumulated charge at the wire end is already included in the previous value of the electric field. Adding the contribution due to the change in charge at the end cap to the electric field at each time step is equivalent to using the total accumulated charge to compute the electric field due to charge, as required in (16).

Both the axial and radial electric fields due to the charge at the wire end cap are rotationally symmetrical. However, there is field variation in the axial direction. In FDTD, the field at the midpoint of a surface is assumed to represent the average field value through that surface [1]. Therefore, we need to average the electric field due to the charged end cap over the respective dual-grid cell facet. We emphasize that it is of utmost importance in FDTD that each field component represents the average value of that field through a cell facet.

The axial electric field at $\Delta z/2$ above the wire end cap is averaged over a dual-grid cell facet of size $\Delta x\Delta y$ as follows:

$$E_{z,\,q}^{\text{ave}} = \frac{1}{\Delta x\Delta y}\int_{-\Delta y/2}^{\Delta y/2}\int_{-\Delta x/2}^{\Delta x/2} E_{z,\,q}(r,\,\Delta z/2)\,dx\,dy \tag{27}$$

where $E_{z,\,q}(r,\,\Delta z/2)$ is given by (25). The averaged value $E_{z,\,q}^{\text{ave}}$ due to charged end cap will be added to the axial electric field computed using the FDTD update equations. Let us then consider the radial electric field in x direction. In order to compute the average value for the radial electric field at $\Delta x/2$ from wire axis, we average the field in axial direction

$$E_{x,\,q}^{\text{ave}} = \frac{1}{\Delta z}\int_{-\Delta z/2}^{\Delta z/2} E_{r,\,q}(\Delta x/2,\,z)\,dz \tag{28}$$

where $E_{r,\,q}(\Delta x/2,\,z)$ is given by (26). The averaged value $E_{x,\,q}^{\text{ave}}$ represents the average radial electric field through a cylindrical surface such as surface S_2 in Fig. 4. Finally, $E_{x,\,q}^{\text{ave}}$ is projected to a dual-grid cell facet using the inverse of the scaling factor of (11). The other radial electric field components at wire end are obtained similarly.

Note that in (26) and (28) we assume that the wire does not block the field contribution of the line charge observed below the wire. However, below the wire end only part of the line charge distributed along the edge of the end cap is "visible" to the observation point. A simple approximation for the masking effect is given by

$$k_M = (1 - a/\Delta) \tag{29}$$

where a is the wire radius and Δ is the transverse cell size. Note that k_M reduces to unity in the limit of an infinitely thin wire.

B. Approximate Solution to Averaging Integrals

Equations (27) and (28) can be evaluated numerically. For the ease of implementation, we provide simple yet satisfactory approximations to (27) and (28). Assuming $\Delta x = \Delta y = \Delta z = \Delta$, the axial electric field due to the charged end cap can be approximated by

$$E_{z,\,q}^{\text{ave}} \approx \left(\frac{\pi}{6} + \sum_{m=1}^{3} c_m(a/\Delta)^m\right)\cdot E_{z,\,q}(0,\,\Delta/2) \tag{30}$$

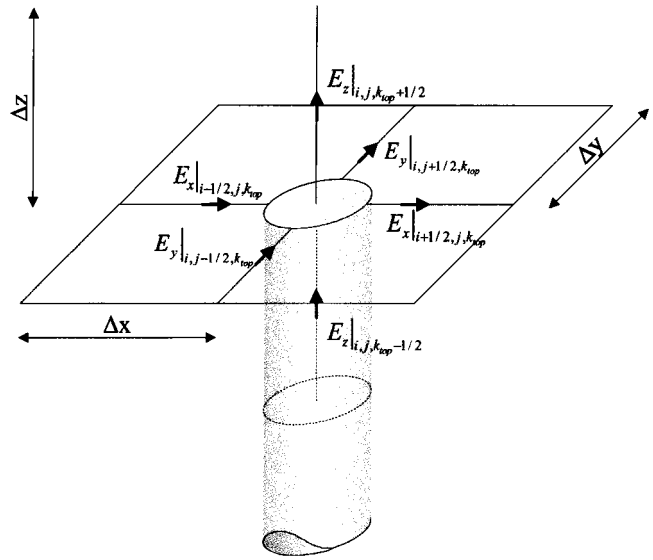

Fig. 6. Electric field components near the wire end. All electric field components shown are affected by the charge at the end cap, except for the axial electric field within the wire at $(i,\ j,\ k_{\rm top}-1/2)$, which is identically set to zero.

where constants $c_1=-0.111$, $c_2=3.31$, and $c_3=-2.51$. The point value of $E_{z,q}$ on the wire axis half a cell above the wire end is given by

$$E_{z,q}(0,\ \Delta z/2)=\frac{\Delta q}{4\pi\varepsilon_0}\,\frac{(\Delta/2)}{\left(a^2+(\Delta/2)^2\right)^{3/2}} \tag{31}$$

where a is the wire radius. This approximation to the equation (27) is accurate within 1% for $a/\Delta<0.5$.

The radial electric field due to the charged end cap can be approximated by

$$E^{\rm ave}_{x,q}\approx\left(\frac{1}{\sqrt{2}}+\sum_{m=1}^{4}c_m(a/\Delta)^m\right)\cdot E_{r,q}\,(\Delta/2,\ 0) \tag{32}$$

where constants $c_1=0.166$, $c_2=-3.65$, $c_3=8.91$, and $c_4=-16.1$. The point value of $E_{r,q}$ computed half a cell from the wire axis in the radial direction is given by

$$E_{r,q}(\Delta/2,\ 0)=\frac{\Delta q}{4\pi\varepsilon_0}\,\frac{(\Delta/2-a)K(k_1)+(\Delta/2+a)E(k_1)}{\pi(\Delta/2)\left((\Delta/2)^2-a^2\right)} \tag{33}$$

where parameter k_1 is given by

$$k_1=\frac{2\sqrt{a(\Delta/2)}}{(\Delta/2)+a}. \tag{34}$$

The data for the elliptic integrals can be found using tabulated data found in [14] or mathematics software such as Maple. Equation (32) provides an approximation to (28) that is accurate within 1% for $a/\Delta<0.4$.

C. Update Equations for Wire End Caps

Let us continue with a z-directed wire in free space, as shown in Fig. 6. The accumulated charge at wire ends contributes to the electric field, resulting in an additional term in electric-field update equations at wire ends. For example, the update equation for the radial field in the x-direction at the top end of the wire is given by

$$\begin{aligned}E_x|^{n+1}_{i+1/2,\,j,\,k_{\rm top}}&=E_x|^{n}_{i+1/2,\,j,\,k_{\rm top}}+(1/k_E)\,k_M\;E^{\rm ave}_{x,q}|^{n+1/2}_{i+1/2,\,j,\,k_{\rm top}}\\&\quad-\frac{\Delta t}{\varepsilon_0\Delta z}\left[H_y|^{n+1/2}_{i+1/2,\,j,\,k_{\rm top}+1/2}-k_H H_y|^{n+1/2}_{i+1/2,\,j,\,k_{\rm top}-1/2}\right]\\&\quad+\frac{\Delta t}{\varepsilon_0\Delta y}\left[H_z|^{n}_{i+1/2,\,j+1/2,\,k_{\rm top}}-H_z|^{n}_{i+1/2,\,j-1/2,\,k_{\rm top}}\right]\end{aligned} \tag{35}$$

where k_E, k_M, and $E^{\rm ave}_{x,q}$ are computed using (11), (29), and (28), respectively. The scaling factor $1/k_E$ projects the radial electric field due to the line charge to a Cartesian dual-cell facet.

The axial electric field component at the wire end also includes an additional term describing the accumulated charge at the wire end. At the top end, we have

$$\begin{aligned}E_z|^{n+1}_{i,\,j,\,k_{\rm top}+1/2}&=E_z|^{n}_{i,\,j,\,k_{\rm top}+1/2}+E^{\rm ave}_{z,q}|^{n+1/2}_{i,\,j,\,k_{\rm top}+1/2}\\&\quad-\frac{\Delta t}{\varepsilon_0\Delta y}\left[H_x|^{n+1/2}_{i,\,j+1/2,\,k_{\rm top}+1/2}-H_x|^{n+1/2}_{i,\,j-1/2,\,k_{\rm top}+1/2}\right]\\&\quad+\frac{\Delta t}{\varepsilon_0\Delta x}\left[H_y|^{n+1/2}_{i+1/2,\,j,\,k_{\rm top}+1/2}-H_y|^{n+1/2}_{i-1/2,\,j,\,k_{\rm top}+1/2}\right]\end{aligned} \tag{36}$$

where the magnetic field components are computed using the standard FDTD update equations. The additional terms in (35) and (36) are assumed small compared to the total electric field. Within this assumption, field variation near the wire can be assumed unaffected by the additional term, and the field component can be used in standard FDTD update equations.

IV. Numerical Results and Discussion

A. Half-Wave Dipole as a Transmitting Antenna

A 0.305-m half-wave dipole antenna was used to test the proposed model. The antenna input resistance and reactance were computed at frequency $f=c/(2L)$, where c is the speed of light and L is the length of the dipole. The proposed model and the standard thin-wire model [1] were tested for a wide range of values for the wire radius. In addition, scattering parameter $|S_{11}|$ to a 50-Ω reference was computed for a thick and thin wire in order to demonstrate how accurately the resonance frequency is predicted.

In FDTD, a uniform grid was used. Two cell sizes were considered with 41 and 21 cells per dipole length L resulting in 7.44- and 14.5-mm cells, respectively. In the proposed model, the straight wire sections were modeled using (10) and (14). At wire ends, (35) and (36) were also used. The computational space extended at least ten cells from the antenna in each direction and was truncated using a perfectly matched layer (PML) (8, P, 0.0001) absorbing boundary [15]. A simple delta-gap hard

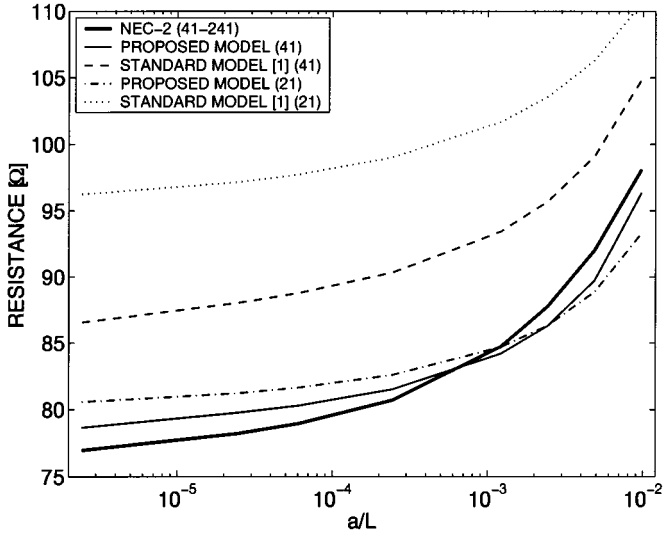

(a)

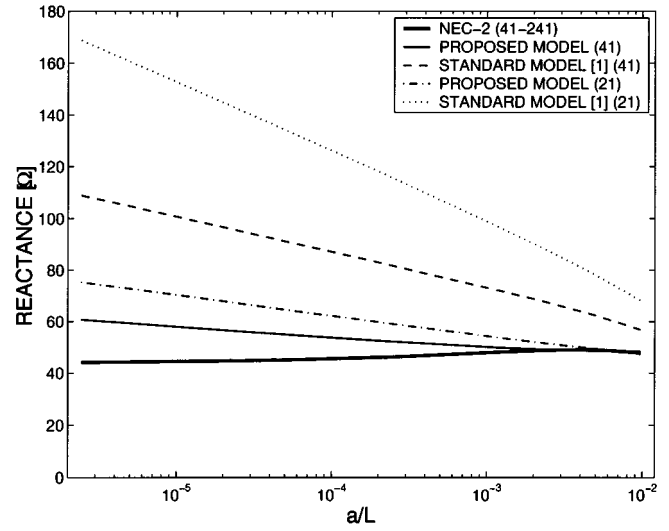

(b)

Fig. 7. Input impedance at frequency $f = c/2L$, where c is the velocity of light in vacuum and L is the length of the dipole. (a) and (b) are plotted as function of wire radius a divided by dipole length L. The number in the legend refers to the number of segments or cells used per antenna length L. (a) Input resistance. (b) Input reactance.

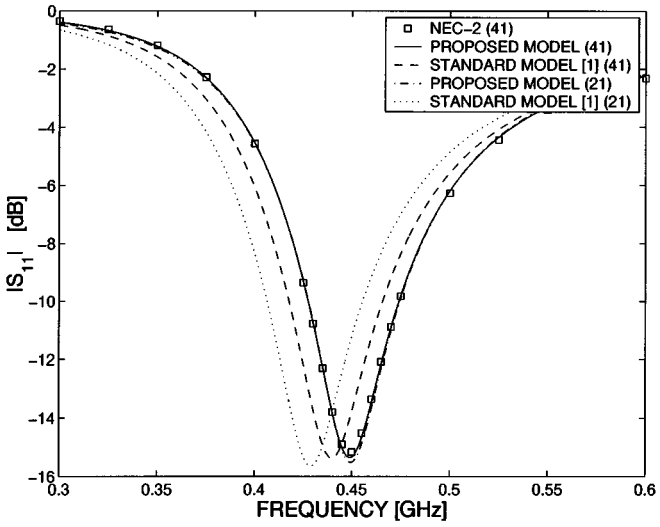

(a)

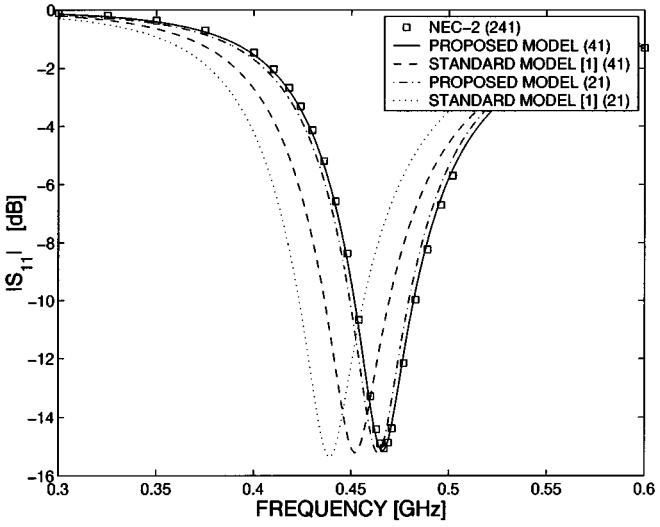

(b)

Fig. 8. $|S_{11}|$ referenced to 50 Ω. The number in the legend refers to the number of segments or cells used per antenna length L. (a) Wire radius $a = 0.4\Delta$, where $\Delta = L/41$. (b) Wire radius $a = 0.05\Delta$, where $\Delta = L/41$.

source was used to excite the antenna [9]. In impedance calculations, the voltage values were interpolated in time to compensate the half a time-step offset between the voltage and current values.

The reference data were computed using NEC-2 [16]. The ratio of the segment length and wire radius should be greater than two when using the extended thin-wire kernel in NEC-2. This limits the number of segments that can be used to model a thick-wire antenna. For example, the smallest number of segments per dipole length used for the thickest antenna was 41, resulting in a ratio of the segment length and wire radius of 2.5. For thinner wires, the number of segments was gradually increased up to 241 segments per dipole length.

The input impedance at frequency $f = c/2L$ is shown in Fig. 7. Using the proposed model, both input resistance in Fig. 7(a) and input reactance in Fig. 7(b) are accurately modeled over a wide range of values for the wire radius. As expected, a dense grid provides more accurate results. As shown in Fig. 8, the resonance frequency of the dipole antenna is very accurately predicted by the proposed model. The results are very accurate for a thick wire [see Fig. 8(a)], while the error is gradually increased, as the wire radius is decreased [see Fig. 8(b)]. The results indicate that the proposed model provides a significant improvement compared to the standard model [1]. The improvement over the standard model is largely due to the end-cap model.

The effect of the end-cap model on $|S_{11}|$ is illustrated in Fig. 9. The dipole is modeled using the standard wire model and the proposed model both with and without the end-cap model. Again, the dipole was modeled using 41 and 21 cells per dipole length L. The results with the standard wire model and the proposed model without the end-cap model suffer from a shift in frequency toward dc. The difference between the results is due to the inconsistent treatment of field components in the standard

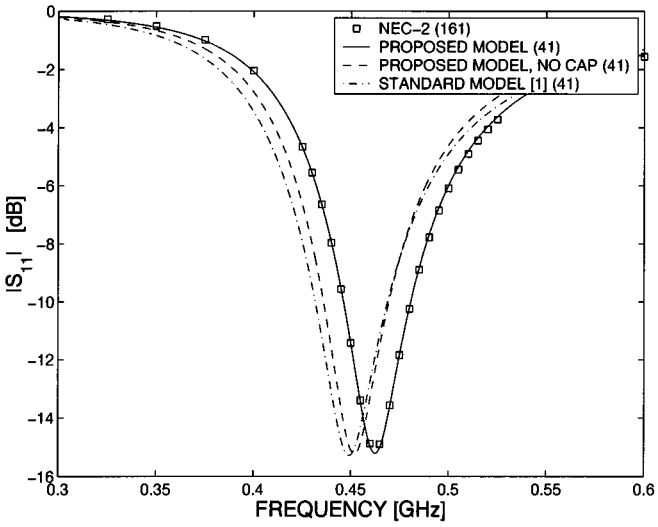

(a)

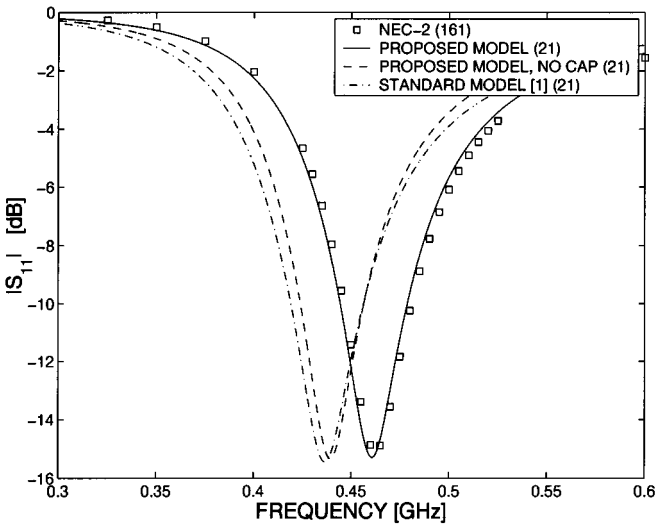

(b)

Fig. 9. Effect of the end-cap model on $|S_{11}|$ of a 0.305-m dipole antenna with wire radius $a = 0.1\Delta$, where $\Delta = L/41$. $|S_{11}|$ is referenced to 50 Ω. The text "NO CAP" in the legend refers to the result computed using the proposed wire model without the end-cap model. The cell size is: (a) $\Delta = L/41$ and (b) $\Delta = L/21$.

wire model. In contrast, a considerable improvement in results is observed when the end-cap model is added to the proposed wire model. For both grid resolutions considered, the results with the end-cap model agree very well with the reference result.

An explanation can be found as follows. In FDTD, PEC objects appear larger than their nominal dimensions [18]. This is also the case with PEC wires where the field singularity results in a loss of the second-order accuracy of the FDTD algorithm [19]. While the wire radius can be accurately controlled using thin-wire models, the length of the wire is affected by the coarseness error [6]. As a result, wires appear longer than their nominal length. In the case of dipole antenna, the error in resonance frequency due to the coarseness error has been shown to dominate the error caused by numerical dispersion [6]. In Fig. 9, both the standard and proposed models without an end-cap model suffer mainly from the coarseness error. In contrast, the end-cap model modifies the fields near wire ends such that the coarseness error in the axial direction is reduced. The results with the end-cap model indicate that part of the error in resonance frequency typically attributed to the dispersion error is, in fact, caused by the coarseness error.

For further verification, the proposed wire model without the end-cap model was compared to a filamentary PEC dipole. The proposed model reduces exactly to a filamentary PEC wire when the nominal wire radius is set to $e^{-\pi/2}\Delta \approx 0.208\Delta$. This is in agreement with the result for a 2-D TM-mode thin-wire model [4], [5], providing further support for validity of the proposed wire model. In contrast, the standard thin-wire model [1] reduces to a filamentary PEC wire when the nominal radius is set to $e^{-2}\Delta \approx 0.135\Delta$ [17].

B. Half-Wave Dipole as a Receiving Antenna

In order to verify the proposed model for a receiving antenna, two 0.305-m dipole antennas 20 cells apart were considered. One antenna was used as a transmitter, while the other was used as a receiver. The antennas were modeled using a uniform grid with 41 cells per dipole length L resulting in 7.44-mm cells. An RVS with a 50-Ω internal resistance was used for excitation, and the receiving antenna was loaded with a 50-Ω resistance [11]. The reference result was computed using NEC-2, utilizing a 50-Ω load in both the transmitting and receiving antennas.

The coupling between antennas with $a = 0.1\Delta$ is shown in Fig. 10. Both magnitude and phase of S_{21} follow closely the reference result, indicating that the proposed model is also valid for receiving antennas. The frequency shift present in the results computed using the standard model [1] is mainly caused by the coarseness error.

C. Application to Waveguide Probe Feed

In addition to simple wire antennas, metal wires are also used as a part of the feed structure. A typical example is the coaxial probe feed that can be used to excite, for example, patch antennas and waveguides. In order to demonstrate the proposed wire model as an important part of the coaxial probe feed structure, we consider input admittance of the probe-fed rectangular waveguide described in [19]. As the effect of the end-cap model is demonstrated in the previous two sections, we seek to illustrate the importance of correct averaging of the field components discussed in Section II.

A cross-sectional view of the waveguide is shown in Fig. 11. The waveguide is matched at both ends in the y-direction and the probe extends to the top of the waveguide. The end-cap model was, therefore, not used with the proposed model. However, in case the probe does not extend to the top of the waveguide, the end-cap model should be included. The waveguide was modeled using a $[18\,20\,20]$ cell grid truncated with the PML(8, P, 0.0001) absorbing boundary [15]. A 50-Ω RVS with a sine-modulated Gaussian pulse centered at time step $n = 600$ utilizing a $1/e$ decay rate of 100 time steps and modulation frequency of 1.5 GHz was used to excite the waveguide. The time step was set to 0.9 times the Courant limit.

The input admittance was computed as given in [21]. The voltage values were interpolated in time to obtain voltage at the same instant of time the current is defined. The input impedance at $\Delta z/2$ above the bottom of the waveguide

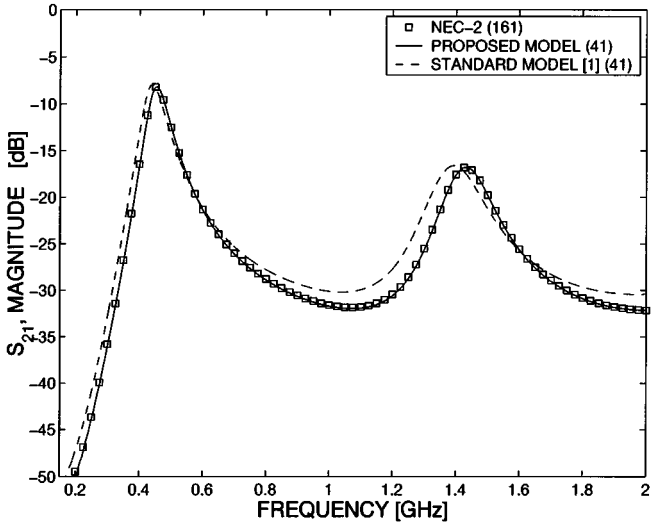

(a)

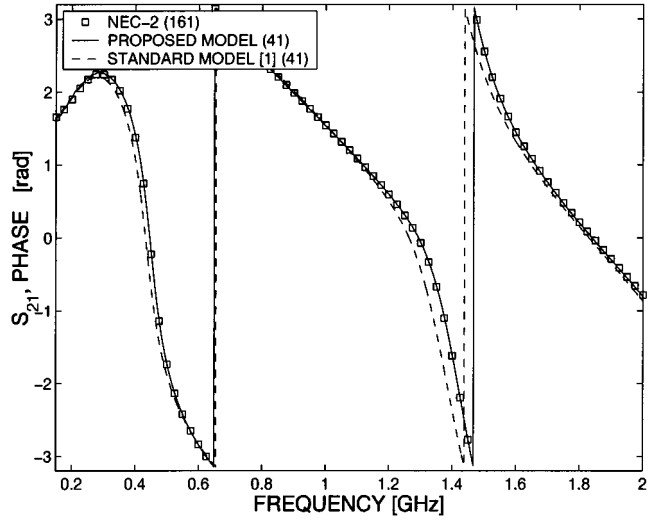

(b)

Fig. 10. S_{21} computed for two dipole antennas with wire radius $a = 0.1\Delta$, where $\Delta = L/41$, located 20 cells apart. (a) Magnitude. (b) Phase.

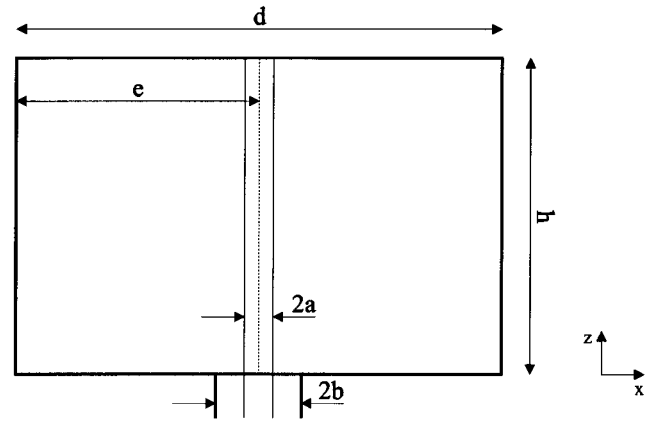

Fig. 11. Cross-sectional view of the coaxial probe feed of a rectangular waveguide. The dimensions are identical to those given in [20], $a = 3.1$ mm, $b = 7.13$ mm, $h = 57$ mm, $d = 135$ mm, and $e/d = 0.5$.

was then computed. Parameter S_{11} referenced to 50 Ω was computed and shifted to the bottom of the waveguide by multiplying by $\exp(-j\omega(\Delta z/2)/c)$. The input impedance (and input admittance) at the bottom of the waveguide was finally computed from the corrected S_{11}.

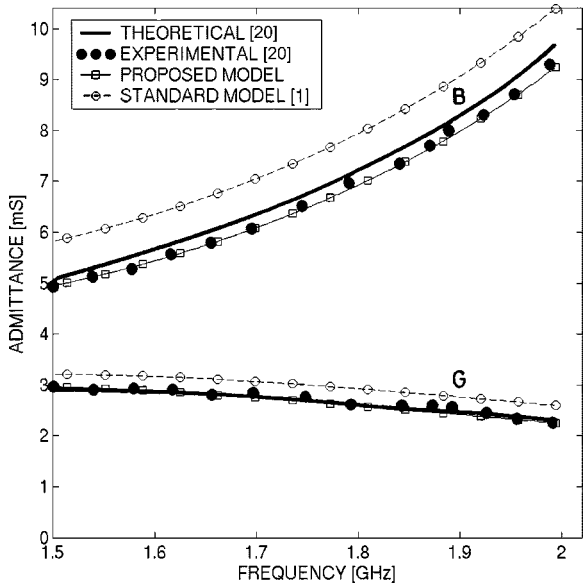

Fig. 12. Input admittance of the waveguide. G and B refer to conductance and susceptance, respectively. The theoretical and experimental data are extracted from [20].

The results are shown in Fig. 12. Both the real and imaginary part of the input admittance are accurately modeled using the proposed model. Comparison to the results with the standard wire model indicates that inconsistent treatment of field components affects the accuracy of the standard model [1]. This is especially the case in the feed region, where the current and voltage computed form field quantities directly affect the computed input admittance. For comparison, the simulation was repeated using the delta-gap hard source to excite the waveguide. The results were identical to those shown in Fig. 12.

D. Stability

An analytical stability condition is not derived for the proposed model. Instead, numerical tests were carried out using both small and large values for a wire radius a. In order to have control over the size of the feed, the feed point was also modeled using the thin-wire equations. A Gaussian pulse centered at time step $n = 200$, utilizing a $1/e$ decay rate of 15 time steps was used as an excitation waveform. The tests were carried out using a uniform grid for a duration of 200 000 time steps.

Using a delta-gap hard source, the proposed model was found stable for wire radii less than $\Delta/2$, where Δ is the transverse cell size. In fact, the proposed model was stable with $a = 0.49\Delta$ and a time step of 0.999 times the Courant limit [9], whereas with the standard model time step needed to be reduced in order to obtain stability with $a = 0.49\Delta$.

As discussed in Section II-C, connecting an RVS on a wire limits the stable range of values for wire radius a and time step Δt. When using an RVS, the time step needed to be reduced to 0.9 times the Courant limit in order to obtain stability with $a = 0.49\Delta$. However, with the standard thin-wire model [1], the time step needed to be reduced even further in order to obtain

stability. This shows that the instability observed when using both a large time step and large wire radius a was not introduced by the proposed model.

V. Conclusion

A new thin-wire model for FDTD has been proposed. The proposed model can be applied to both connected and unconnected wires. Special care is taken when connecting straight wire sections to a Cartesian FDTD grid. In addition, an end-cap model based on conservation of charge and Coulomb's law to treat unconnected wire ends has been proposed. The stability of the model was investigated using numerical tests. The tests indicate that the model is stable for wire radii less than $\Delta/2$, where Δ is the transverse cell size.

The model was evaluated by comparison to NEC-2 data using a dipole antenna as a test structure. The results indicate that the proposed model can be used to accurately model both transmitting and receiving antennas. In addition, the proposed model was applied to a waveguide problem to demonstrate validity of the wire model as a part of a feed structure.

Acknowledgment

The authors would like to thank Prof. A. G. Williamson, Department of Electrical and Electronic Engineering, University of Auckland, Auckland, New Zealand, for his permission to reproduce theoretical and experimental results for input admittance of a probe-fed rectangular waveguide, which was originally published in [20].

References

[1] A. Taflove, K. Umashankar, B. Beker, F. Harfoush, and K. Yee, "Detailed FD-TD analysis of electromagnetic fields penetrating narrow slots and lapped joints in thick conducting screens," *IEEE Trans. Antennas Propagat.*, vol. 36, pp. 247–257, Feb. 1988.

[2] M. Douglas, M. Okoniewski, and M. Stuchly, "Accurate modeling of thin-wire antennas in the FDTD method," *Microwave Opt. Technol. Lett.*, no. 4, pp. 261–265, May 1999.

[3] I. J. Craddock and C. J. Railton, "A new technique for the stable incorporation of static field solutions in the FDTD method for the analysis of thin wires and narrow strips," *IEEE Trans. Microwave Theory Tech.*, pp. 1091–1096, Aug. 1998.

[4] G. Waldschmidt and A. Taflove, "The determination of the effective radius of a filamentary source in the FDTD mesh," *IEEE Microwave Guided Wave Lett.*, vol. 10, pp. 217–219, June 2000.

[5] R. Mäkinen, J. Juntunen, and M. Kivikoski, "An accurate 2-D hard-source model for FDTD," *IEEE Microwave Wireless Comp. Lett.*, vol. 11, pp. 74–76, Feb. 2001.

[6] ——, "Coarseness error in FDTD thin-wire models," in *Proc. IEEE AP-S Int. Symp.*, vol. 4, Boston, MA, July 8–13, 2001, pp. 158–161.

[7] G. J. Burke, "Numerical electromagnetics code—NEC-4 method of moments—Part II," Lawrence Livermore Nat. Lab., Livermore, CA, Tech. Rep. UCRL-MA-109338-PT-2, Jan. 1992.

[8] R. Mäkinen and M. Kivikoski, "Stability of FDTD source models when connected on a wire described by thin-wire equations," in *Proc. 8th Int. Microwave Opt. Technol. Symp.*, Montreal, QC, Canada, June 19–23, 2001, pp. 245–248.

[9] A. Taflove, *Computational Electrodynamics: The Finite-Difference Time-Domain Method*. Norwood, MA: Artech House, 1995.

[10] W. Sui, D. A. Christensen, and C. H. Durney, "Extending the two-dimensional FDTD method to hybrid electromagnetics system with active and passive lumped elements," *IEEE Trans. Microwave Theory Tech.*, vol. 40, pp. 724–730, Apr. 1992.

[11] M. Picket-May, A. Taflove, and J. Baron, "FD-TD modeling of digital signal propagation in 3-D circuits with passive and active loads," *IEEE Trans. Microwave Theory Tech.*, vol. 42, pp. 1514–1523, Aug. 1994.

[12] J. A. Stratton, *Electromagnetic Theory*. New York: McGraw-Hill, 1941.

[13] A. Salinas, R. G. Martin, A. R. Bretones, and I. S. Garcia, "Modeling of straight thin wires using time-domain electric field integral equations," *Proc. Inst. Elect. Eng.*, pt. H, vol. 141, pp. 123–126, Apr. 1994.

[14] H. B. Dwight, *Tables of Integrals and Other Mathematical Data*, 4th ed. New York: Macmillan, 1961.

[15] J.-P. Berenger, "Three-dimensional perfectly matched layer for the absorption of electromagnetic waves," *J. Comput. Phys.*, vol. 127, pp. 363–379, 1996.

[16] G. J. Burke and A. J. Poggio, "Numerical electromagnetics code (NEC)—Method of moments—Part I," Lawrence Livermore Nat. Lab., Livermore, CA, Tech. Rep. UCID-18 834, Jan. 1981.

[17] S. Watanabe and M. Taki, "An improved FDTD model for the feeding gap of a thin-wire antenna," *IEEE Microwave Guided Wave Lett.*, pp. 152–154, Apr. 1998.

[18] K. S. Kunz and R. J. Luebbers, *The Finite Difference Time Domain Method for Electromagnetics*. Boca Raton, FL: CRC Press, 1993, ch. 3.

[19] G. Mur, "The modeling of similarities in the finite-difference approximation of the time-domain electromagnetic field equations," *IEEE Trans. Microwave Theory Tech.*, vol. MTT-29, pp. 1073–1077, Oct. 1981.

[20] A. G. Williamson, "Analysis and modeling of a coaxial-line/rectangular-waveguide junction," *Proc. Inst. Elect. Eng.*, pt. H, vol. 129, pp. 262–270, Oct. 1982.

[21] J. Juntunen, "Note on the S_{11}-parameter and input impedance extraction in antenna simulations using FDTD," *Microwave Opt. Technol. Lett.*, vol. 28, no. 1, pp. 8–11, Jan. 2001.

Riku M. Mäkinen (M'01) was born in Jyväskylä, Finland, in 1970. He received the M.Sc. degree in electrical and electronic engineering (with distinction) from the Tampere University of Technology (TUT), Tampere, Finland, in 1996, and is currently working toward the Dr.Tech. degree at the Institute of Electronics, TUT.

He is currently with the Finnish Graduate School for Electronics, Telecommunications and Automation (GETA).

Jaakko S. Juntunen (M'00) was born in Tornio, Finland, in 1971. He received the Master of Science degree in technical mathematics, Licentiate of Technology degree in electrical engineering, and Doctor of Science degree in electrical engineering from the Helsinki University of Technology (HUT), Helsinki, Finland, in 1995, 1998 and 2001, respectively.

He then joined the Aplac Solutions Corporation, Helsinki, Finland, where he is involved with customer support and training. From 1996 to 2000, he was with the Finnish Graduate School for Electronics, Telecommunications and Automation (GETA). For the academic year 1998–1999, he was with the Aristotle University of Thessaloniki, Thessaloniki, Greece. His research interests are the FDTD method, and the high-order finite-element method applied to electromagnetic problems.

Dr. Juntunen was the recipient of a 1998–1999 European Union Marie Curie Fellowship.

Markku A. Kivikoski (S'77–M'82) was born in Tampere, Finland, on May 13, 1952. He received the Diploma Engineer (M.Sc.), Licentiate of Technology, and Doctor of Technology degrees in electrical engineering from the Tampere University of Technology (TUT), Tampere, Finland, in 1976, 1980, and 1985, respectively.

From 1976 to 1984, he was Assistant, Head Assistant, Research Scientist, Laboratory Engineer, Senior Research Scientist, and Acting Associate Professor with the Helsinki University of Technology (HUT), Helsinki, Finland. From 1984 to 1988, he was Research and Development Manager, Head of Section, and Technical Director with Hollming Ltd. Electronics. From 1988 to 1994, he was with the Technical Research Centre of Finland (VTT) as a Professor and Director of the Machine Automation Laboratory, and a Research Professor and Head of Machine Automation Research. In 1994, he became the Professor Chair of Industrial Electronics with TUT. Since 1996, he has also been the Head of the Institute of Electronics, TUT. In 1998, he became the Head of the Department of Electrical Engineering and a member of the Administrative Board, TUT. His research interests include wireless data transfer for industrial environment, electromagnetic compatibility, embedded real-time systems, and mechatronics.

Dr. Kivikoski serves on the Research Council for Natural Sciences and Engineering, the Academy of Finland.